論文 / 著書情報
Article / Book Information

Title	3D simulation of all-solid-state batteries with real electrode structures derived from X-ray computed tomography
Authors	K. Lee, K. Yanagi, T. Arashi, M. Kodama
Citation	Journal of Power Sources, Vol. 654, No. 30,
Pub. date	2025, 7
DOI	https://dx.doi.org/10.1016/j.jpowsour.2025.237821
Creative Commons	Information is in the article.

Journal of Power Sources 654 (2025) 237821

Contents lists available at ScienceDirect

Journal of Power Sources

journal homepage: www.elsevier.com/locate/jpowsour

3D simulation of all-solid-state batteries with real electrode structures derived from X-ray computed tomography

K. Lee [a], K. Yanagi [b], T. Arashi [b], M. Kodama [a,*]

[a] Institute of Science Tokyo, 2-12-1 Ookayama, Meguro-ku, Tokyo, 152-8550, Japan
[b] Idemitsu Kosan Co., Ltd., 1280 Kamiizumi, Sodegaura, Chiba, 299-0293, Japan

HIGHLIGHTS

- Electrode structure and performance were analyzed by 3D simulation with X-ray CT.
- 3D simulation with real AM structure provides higher accuracy than P2D simulation.
- Smaller AM particles support higher Li diffusion, which leads to higher capacity.
- Larger AM particles accumulate Li only on the surface, suppressing Li diffusivity.
- Not just AM particle size, size distribution is important for battery performance.

GRAPHICAL ABSTRACT

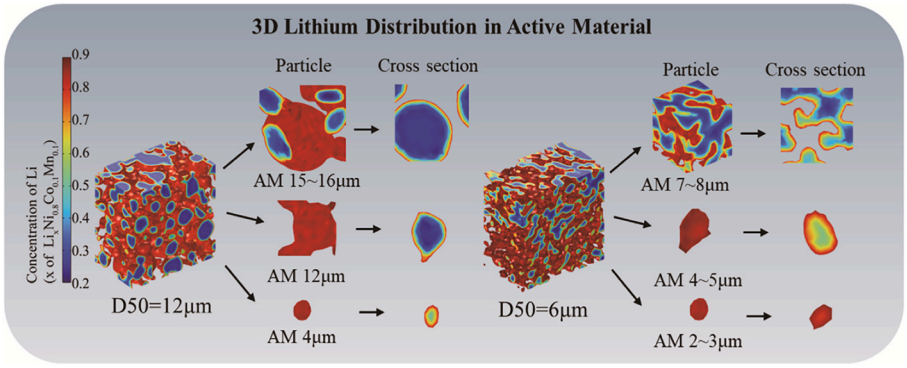

ARTICLE INFO

Keywords:
All-solid-state lithium-ion battery
3D simulation
X-ray computed tomography
Li diffusion
Active material particle size

ABSTRACT

To enhance all-solid-state battery performance, optimization of the electrode structure through highly accurate simulations is essential. However, conventional pseudo-two-dimensional simulations are limited in accuracy, and three-dimensional (3D) simulations have rarely been studied owing to the computational cost and challenges in reproducing the actual electrode structure. In this study, we perform 3D simulations using a finite element method that incorporates the actual electrode structure obtained from X-ray computed tomography images. The 3D simulation reproduced experimental results more accurately than the pseudo-two-dimensional simulation, particularly in capturing the gradient of discharge curves associated with lithium diffusion in the active material (AM), especially at high C-rates. This improvement is attributed to the 3D simulation's ability to account for the AM particle size distribution. Moreover, results from the 3D simulations show that relatively smaller AM particles exhibit higher lithium diffusion efficiency, enabling higher capacity among these particles. Conversely, relatively larger AM particles accumulate high lithium concentrations only on the particle surface, thereby reducing cell performance. These findings reveal that the AM particle size and particle size distribution are key factors in battery performance. Moreover, our approach is expected to accelerate the development of high-performance batteries leveraging 3D simulations.

* Corresponding author.
E-mail address: kodama.m.d0f2@m.isct.ac.jp (M. Kodama).

https://doi.org/10.1016/j.jpowsour.2025.237821
Received 10 March 2025; Received in revised form 17 June 2025; Accepted 1 July 2025

1. Introduction

As the electric vehicle market expands, the development of high-performance and high-safety batteries has become crucial. For example, conventional lithium-ion batteries have a serious risk of ignition because they rely on flammable organic electrolytes [1,2]. Notably, all-solid-state lithium-ion batteries (ASSLiBs) are expected to be used in next-generation technologies because they use non-flammable solid electrolytes (SEs) that are highly stable [3]. Furthermore, ASSLiBs can achieve high energy density because lithium metal is directly used in the anode and minimizes the cooling system volume in the vehicles [4,5]. However, like other batteries, ASSLiBs face the challenge of capacity degradation during rapid charging and discharging. To address this issue, lithium-ion transport in the SE, electrochemical reactions at the SE-active material (AM) interface, and lithium diffusion in the AM must be improved through electrode structure optimization. Nevertheless, optimizing the electrode structure is challenging with experimental approaches alone owing to the complex interplay of material characteristics and internal phenomena of each material. Therefore, various studies have examined the relationship between electrode structure and ASSLiB performance by employing simulations [6–17], predominantly using the pseudo-two-dimensional (P2D) and three-dimensional (3D) models.

Newman et al. applied structural parameters, including the tortuosity and volume fraction of battery materials, in P2D simulations [6–8]. Tortuosity is related to the transport distance of lithium ions and electrons within the AM and SE, respectively. An increase in tortuosity indicates longer transport distances of lithium ions and electrons. Therefore, P2D simulations with tortuosity are used to evaluate battery performance by considering the ohmic overpotential due to their reliable ionic conductivity. In a more advanced approach, Iwamoto et al. incorporated not only these parameters but also the specific contact area diameter (D_{SCA}) measured by X-ray computed tomography (CT) into P2D simulations [9]. The D_{SCA} parameter reflects AM aggregation in the cathode, meaning that the activation overpotential at the AM-SE interface and the diffusion resistance in the AM particles can be considered more accurately. In a previous study, P2D simulations with D_{SCA} revealed that atomizing the AM particle size reduces AM aggregation, shortens the lithium diffusion distance in the AM, and increases battery capacity [10]. However, P2D simulations cannot account for variations in AM particle size and shape because a uniform AM particle size is assumed based on the D_{SCA}, limiting their accuracy and precision.

Although several studies have focused on 3D simulations of ASSLiB performance, few have been reported [11–17]. Bielefeld et al. demonstrated that smaller AM particles enhance the electronic conductivity in composite cathodes by increasing the surface area available for particle connections [11]. They also highlighted the adverse effects of polymeric binders on ionic conductivity and active surface area, emphasizing the need to optimize binder content for higher electrode performance [12]. M. So et al. employed the discrete element method to simulate the compaction of cathodes in ASSLiBs, analyzing the impacts of solid electrolyte coatings on ionic transport, electrode performance, and mechanical damage [13]. Yamakawa et al. used phase-field modeling and neural network regression to investigate the impact of cathode microstructure on the high-rate discharge capacity in ASSLiBs [14]. In these papers, the cell components were initialized as spheres, meaning that particle shape deviations were not considered. In contrast, Huang et al. modeled the electrochemo-mechanical response of ASSLiBs using 3D reconstructions, revealing the effects of interfacial stability and diffusion-induced stress on battery performance [15]. Fathiannasab et al. simulated the spatial distribution of electrochemical properties in ASSLiBs using a 3D reconstructed electrode model and demonstrated how pressing pressure affects lithium-ion uniformity and battery performance [16]. Finsterbusch et al. identified reactions at the cathode-SE interface as the primary limitation in garnet-based ASSLiBs, proposing optimization strategies based on experiments and 3D microstructure modeling [17]. However, only a small region of the electrode was reconstructed in these studies, limiting the amount of AM considered within the simulations. Furthermore, most studies did not directly compare the simulation results with experimental data, lacking quantitative validation [11–16]. Even if a quantitative comparison was conducted, structural differences between the actual and simulated electrodes may arise because the expected performance of the entire electrode was modeled based on the behavior of a small portion, which was done to reduce the computational cost [17].

Using real electrode structures over larger regions remains rare among studies focused on 3D simulations, although considering particle size and shape variations in the AM across a large electrode region is critical for achieving high-precision simulations. On the basis of this understanding, we conducted 3D simulations of ASSLiBs with real electrode structures obtained from X-ray CT. The AM's particle shape and size deviations were observed by X-ray CT, and the electrode was reconstructed as a whole in the thickness direction, not just a part. The 3D simulation results were compared with experimental results obtained under the same conditions to validate their accuracy. Additionally, these results elucidated how changes in the median AM particle diameter ($D50_{AM}$) affect battery performance. This study aims to confirm the effectiveness of 3D simulations based on real electrode structures obtained from X-ray CT images and demonstrate their design potential for improving ASSLiB performance.

2. Experimental and numerical procedures

Experimental and numerical methods were conducted to confirm the validity of 3D simulations and elucidate the lithium diffusion characteristics in actual electrodes. Herein, cathodes with two different median AM particle diameters ($D50_{AM}$) were prepared using $Li_4Ti_5O_{12}$-coated $LiNi_{0.8}Co_{0.1}Mn_{0.1}O_2$ as AM particles ($D50_{AM}$ = 6 or 12 μm), Li-argyrodite as SE particles (Idemitsu Kosan, D50 = 1 μm), and a conductive additive (DENKA BLACK). The AM, SE, and conductive additive were combined in proportions of 75, 22, and 3 wt%, respectively. The volume fraction of AM, SE and void were 0.46, 0.44 and 0.1 respectively. The AM and SE volume fractions were calculated based on true densities, weight fractions, and void fractions.

In the experimental approach, X-ray CT analysis and discharge experiments were performed to evaluate battery performance. For numerical methods, P2D and 3D simulations were conducted, and X-ray CT images of the electrode structure were acquired to support both simulation approaches. The 3D and P2D simulation results were then compared with the experimental results to assess their validity. Then, we discussed internal phenomena, such as lithium diffusion, in real electrode structures using these 3D simulation results.

2.1. Experimental procedures

2.1.1. X-ray CT measurement

X-ray CT measurements were conducted for the two cathode samples with different AM particle sizes. Samples were pressed into pellets by molding 12 mg of cathode composites at 200 MPa. This compression pressure is within the typical range used in ASSLiB studies and is not anticipated to induce significant structural alterations or distortions. To improve X-ray transmission and achieve high-resolution X-ray CT images, the pellets were punched into 0.3 mm diameter disks using a hand punch (NOGAMI). The 0.3 mm cathode samples were placed in air-tight jigs with molecular sieves (type 3A, Kanto Chemical), which were used to absorb water vapor within the jig's internal gas space [18]. The air-tight jigs were made of polyetheretherketone, a material with a high X-ray transmission ratio [18,19]. All procedures, from compression to installation in the jig, were performed in an argon-filled glove box with a low dew point (<−80 °Cdp).

X-ray CT imaging of the cathode samples was performed by scanning through 360° using an X-ray CT system (Rigaku, customized nano3DX)

with a molybdenum target, tube voltage of 45 kV, and current set to 66 mA [10]. For each cathode type, 1000 images were captured with an exposure time of 30 s per image. CT reconstructed images (325 nm × 325 nm × 325 nm voxel size) were generated from the series of transmission images. In the X-ray CT images, the AM and SE regions were distinct.; the AM particles appeared white, whereas the SE and void regions appeared black as shown later in Fig. 1 (1) and Fig. 2 (1). This contrast occurs because the X-ray absorption coefficient is higher for the AM than for the SE and void regions. The voids are small and have low resolution, mainly contained within the SE region. In addition, the X-ray CT images acquired in this study showed clear shapes of AM particles and SEs, and no structural destruction or distortion due to compression was observed at 200 MPa compression.

2.1.2. Cathode half-cell discharge experiment

Two cathode cells with different AM particle sizes were assembled to perform discharge experiments. First, a cell comprising a 10 mm diameter Macor cylinder and a stainless-steel cathode current collector was filled with 90 mg of SE (i.e., Li-argyrodite, ionic conductivity of 3.5 mS/cm), which was then compressed at 185 MPa. Next, 14.1 mg of the same cathode composite used for the X-ray CT measurements was placed on the SE layer and compressed at 555 MPa. Through these processes, the SE layer and cathode layer were fabricated with thicknesses of 430 and 43 μm, respectively. The thickness of the SE and cathode layers were measured by using a micrometer after the cathode half-cell was removed from the jig. The thickness variation of both SE and cathode layers was less than 2 %, confirming good reproducibility in several samples. In addition, deformation with 200 MPa compression is estimated to be less than 1 % because Young's modulus of both the AM and sulfide SE exceed 20 GPa. Therefore, the deviation in thickness measurement under non-pressurized condition is considered negligible. Lastly, lithium foil was positioned as the counter electrode and compressed at 93 MPa, completing the cell. Different compression procedure was the result of optimizing for different material properties and purposes. As mentioned above, the SE was first compressed to fabricate SE layer as a temporary forming pressure. Then the cathode composite powder was placed on the SE layer, and they were pressed to bond well at the interface by interspersing temporary molding process. On the other hand, since the lithium foil is a soft material, it was finally bonded at a relatively low surface pressure to both retain its shape and ensure contact. These procedures were all conducted in a glove box filled with argon and maintained at a low dew point (<−80 °Cdp). Finally, the completed cells were used to perform discharge experiments under a constant current ranging from 0.189 to 15.12 mA (0.1–8C) and a potential range of 4.2 to 3.2 V vs. Li^+/Li. The discharge experiments were conducted after the assembled cells rested for 10 h. Moreover, the assembled cell underwent electrochemical conditioning consisting of two 0.1C charge-discharge cycles for 40-h period to stabilize the interface.

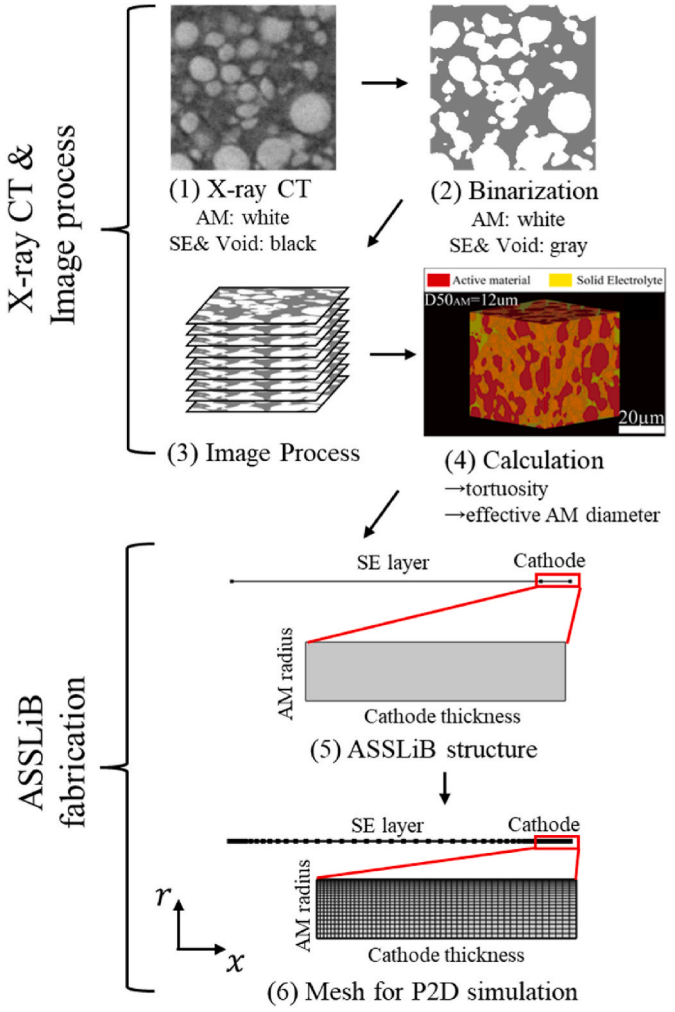

Fig. 1. Structural data import and meshing process used to construct the P2D simulation model from X-ray CT images. (1) electrode structure measured by X-ray CT images, AM: white, SE and void: black, (2) Binarization on X-ray CT image, AM: white, SE and void: gray, (3) fabrication of electrode structure by image process, (4) calculation of the structural parameters such as tortuosity (τ) and effective AM diameter (D_{SCA}), (5) fabrication of ASSLiB structure used in P2D simulation, 1D: entire ASSLiB structure, 2D: electrode structure, (6) mesh of ASSLiB structure for simulation.

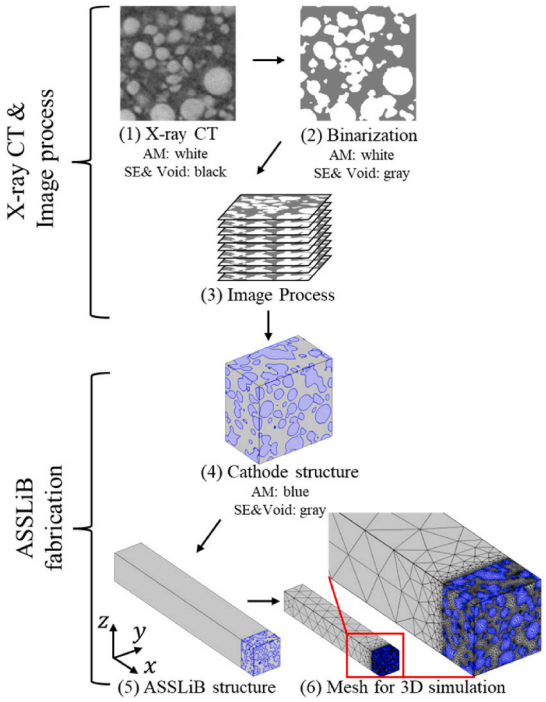

Fig. 2. Structural data import and meshing process used to construct the 3D simulation model from X-ray CT images. (1) electrode structure measured by X-ray CT images, AM: white, SE and void: black, (2) Binarization on X-ray CT image, AM: white, SE and void: gray, (3) fabrication of AM structure by image process, (4) fabrication of electrode directly applied to actual AM structure, (5) fabrication of ASSLiB structure used in 3D simulation, (6) mesh of ASSLiB structure for simulation.

2.2. Numerical procedures

First, the common calculation methods and parameters used for P2D

simulations and 3D simulations are described, and then the numerical simulations for each model are demonstrated.

2.2.1. Common features of the P2D and 3D ASSLiB models

The P2D and 3D ASSLiB models were constructed based on the structural conditions used in the discharge experiments. The common parameters of these models are shown in Table 1, which were not obtained from the CT images. The cathode thickness ($L_{cathode}$) was 43 μm, and the volume fractions of AM (ϵ_{AM}), SE (ϵ_{SE}) and void (ϵ_{Void}) were 0.46, 0.44, and 0.1, respectively. The thickness of the SE layer ($L_{SE\ layer}$) was 450 μm. Several governing equations were employed at the lithium foil-SE interface, SE, AM-SE interface, and AM in these two simulations. First, the Butler–Volmer equation was used at the lithium foil-SE interface.

$$i_{Li-SE} = i_{0a}\left[exp\left(\frac{\alpha F\eta}{RT}\right) - exp\left(\frac{-\alpha F\eta}{RT}\right)\right] \quad (1)$$

α, i_{Li-SE}, i_{0a}, F, and η represent the reaction transfer coefficient, current density at the lithium foil-SE interface, exchange current density at the anode, Faraday constant, and activation overpotential, respectively. The α value was set at 0.5, and the exchange current density at the anode, i_{0a}, was set at 22.5 A/m^2. The batteries used in experiments were small, and the effect of heat generation was negligible, meaning that the battery temperature was approximately constant at room temperature. Therefore, T was set at 298 K. In this study, the small cell (Φ10 mm) used for discharge experiments was pressed and enclosed within a large stainless-steel jig, which served as an effective heat sink. While heat generation is expected at high current densities such as 8C, the thermal mass and high thermal conductivity of the jig ensured rapid heat dissipation. From the discharge experiment, no significant temperature rise was detected during high-rate discharge, supporting the assumption of isothermal conditions at 298 K.

Next, the Nernst–Planck and Maxwell equations for the SE were used.

$$\nabla \times \vec{E} = 0 \quad (2)$$

$$\vec{E} = -grad(\phi) \quad (3)$$

$$\nabla \cdot \vec{j} = 0 \quad (4)$$

$$\vec{E} = \frac{\epsilon_{SE}}{\tau}\sigma \cdot \vec{j} \quad (5)$$

$$boundary\ condition: \ \varnothing|_{Li-SE\ interface} = 0, \left.\frac{\partial \varnothing}{\partial x}\right|_{cathode\ C.C.} = 0$$

$\vec{E}$, ϕ, $\vec{j}$, ϵ_{SE}, σ and τ are the electrical field intensity vector, ionic electrical potential, current density vector, volumetric fraction of the SE, ionic conductivity of the SE, and tortuosity of the SE, respectively. The ion conductivity of SE was set at 3.5 mS/cm, as observed in the discharge experiments [20]. In the P2D simulation, the SE tortuosity was directly substituted for the value calculated from the X-ray CT image. However, in the 3D simulation, the SE tortuosity was determined using the Bruggeman correlation, $\tau = {\epsilon_{SE}}^{-1/2}$ to consider the effect of voids in the SE [21]. Since the resolution of CT images is limited, voids within the SE cannot be clearly distinguished and are instead treated as part of the SE. To account for the effect of these unresolved voids, Bruggeman correlation was used to estimate the tortuosity of the SE-void mixture and corrected the ionic conductivity accordingly. In the boundary condition equation, x denotes the thickness direction of the ASSLiB.

The electrochemical reaction at the SE-AM interface was calculated using the Butler–Volmer equation.

$$i_{AM-SE} = i_{0c}\left[exp\left(\frac{\alpha F\eta}{RT}\right) - exp\left(\frac{-\alpha F\eta}{RT}\right)\right] \quad (6)$$

α, F, and η indicate that the reaction transfer coefficient, Faraday constant, and activation overpotential, similar to equation (1). i_{AM-SE} and i_{0c} refer to the current density at the SE-AM interface and exchange current density at the cathode, respectively. The α value was also set at 0.5, and the exchange current density at the cathode, i_{0c}, was set at 1 A/m^2 [22]. T was set at 298 K for the same reason as in equation (1).

Lithium diffusion in the AM was calculated using the following equation.

$$\frac{\partial c}{\partial t} + \nabla \cdot (-D\nabla c) = 0 \quad (7)$$

c and D are the lithium concentration and diffusion coefficient in the AM, respectively. The maximum value of c (c_{max}) was 55,000 mol/m^3. The lithium diffusion coefficient in the AM (D) was set at 2.9 × 10^{-15} m^2/s [23]. This value was determined using the muon spin relaxation method and was chosen for the 3D simulations. Moreover, the use of a liquid electrolyte increases the apparent diffusion coefficient because of its penetration into cracks in the AM [24]. Therefore, the diffusion coefficient was measured in the AM without using a liquid electrolyte.

These equations were solved for the two simulation models using meshes. For each mesh, an instantaneous solution (i.e., for the lithium concentration, ionic potential, and electronic potential) was obtained by solving a system of linear equations discretized using the Galerkin finite element method with the conjugate gradient method. Furthermore, by expanding the time evolution equations and solving them in a non-stationary manner, we calculated the variation in each distribution as the discharge reaction progressed. The P2D and 3D simulations were performed using COMSOL Multiphysics (V6.2) software with a battery design module.

2.2.2. Numerical simulation using the P2D ASSLiB model

The P2D simulations were performed as previously described [10]. Fig. 1 illustrates the procedures used to construct the P2D simulation model with X-ray CT. The SE tortuosity and AM specific contact area diameter (D_{SCA}) were calculated to build P2D ASSLiB models. SE tortuosity can be used to estimate the lithium-ion transport characteristics in SE [10]. D_{SCA} refers to the AM diameter of a sphere, indicating the AM-SE interfacial area and the degree of AM particle aggregation. These structural parameters were acquired from the CT images of the electrode structure, which was generated in 3D through binarization and image processing (Fig. 1(2) and (3)). Then, the SE tortuosity values were computed by electric field analysis using the 3D electrode structure [25,26]. D_{SCA} values were determined from the AM-SE interface area and the corresponding AM particle volumes in 3D structures (Fig. 1(4)). These parameters are shown in Table 2. SE tortuosity (τ) was 1.61 in the electrode with $D50_{AM}$ = 6 μm and 1.46 in the electrode with $D50_{AM}$ = 12 μm. AM specific contact area diameter (D_{SCA}) was 12.2 μm in the electrode with $D50_{AM}$ = 6 μm and 19.5 μm in the electrode with $D50_{AM}$ = 12 μm. Using these structural parameters, the lithium-ion transportation in the SE and the electrochemical reactions at the AM-SE interface were calculated in a one-dimensional (1D) battery model,

Table 1
Parameters used for P2D and 3D simulations.

Parameter		Value
i_{0a}	Exchange current density in anode	22.5 A/m^2
i_{0c}	Exchange current density in cathode	1 A/m^2
α	Reaction transfer coefficient	0.5
ϵ_{SE}	SE volume fraction	0.46
ϵ_{AM}	AM volume fraction	0.44
ϵ_{Void}	Void volume fraction	0.1
σ	Ionic conductivity of SE	3.5 mS/cm
c_{max}	Maximum lithium concentration in AM	55,000 mol/m^3
D	Lithium diffusion coefficient in AM	2.9 × 10^{-15} m^2/s
$L_{cathode}$	Thickness of cathode	43 μm
$L_{SE\ layer}$	Thickness of SE layer	450 μm

Table 2
Parameters used for P2D simulation.

Parameter		Value from X-ray CT
τ	SE tortuosity	1.61 ($D50_{AM}$ = 6 μm) 1.46 ($D50_{AM}$ = 12 μm)
D_{SCA}	AM specific contact area diameter	12.2 μm ($D50_{AM}$ = 6 μm) 19.5 μm ($D50_{AM}$ = 12 μm)

using the x-axis as the cell thickness direction. From this model, lithium diffusion in the AM was calculated in a 2D cathode model, using the x-axis as the cathode thickness direction and the y-axis as the AM particle radius (Fig. 1(5)). In the 1D model, the minimum and maximum element sizes of the mesh were approximately set at 4.78×10^{-6} and 1.82×10^{-5} m, respectively, and the maximum element growth rate was 1.25. In the 2D model, the minimum and maximum element sizes of the mesh were approximately set at 1.15×10^{-6} and 1.02×10^{-7} m, respectively, and the maximum element growth rate was set at 1.3 (Fig. 1(6)). Therefore, 46 elements were used for the 1D model and 1000 elements for the 2D model for both 6 μm and 12 μm AM particles. The mesh convergence has already been investigated in a previous study of P2D simulation [10]. After this process, P2D simulations were performed using the governing equations mentioned in Section 2.2.1. The following boundary condition was used in equation (7), for calculating lithium diffusion in the AM.

$$\left.\frac{\partial c}{\partial r}\right|_{r=0} = 0 \tag{8}$$

r is the AM radius, and $r = 0$ indicates the center of the AM particle.

2.2.3. Numerical simulation using the 3D ASSLiB model

Fig. 2 illustrates the procedures used to construct the 3D simulation model with X-ray CT. Notably, the discharge simulations were conducted by applying the actual electrode structure to the 3D ASSLiB model. The AM structures were obtained through binarization and image processing, using X-ray CT images (Fig. 2(2) and (3)). Then, the obtained AM structures were filled with SE (Fig. 2(4)). In Fig. 2(4), the AM parts are shown in blue, and the SE parts are shown in gray. The total 3D ASSLiB structure was generated by combining these electrodes with lithium foil and the SE layer (Fig. 2(5)). The tetrahedral mesh is demonstrated in Fig. 2(6). Here, the mesh is rough because the SE layer only allows lithium ions to flow toward the cathode, but the mesh is finer in the cathode because various reactions take place at the AM-SE interface and in the AM. The minimum and maximum element sizes of the tetrahedral mesh in the SE layer were approximately set at 2.88×10^{-8} and 4.97×10^{-5} m, respectively, and the maximum element growth rate was 1.5. The minimum and maximum element sizes of the tetrahedral mesh in the cathode were approximately set at 1.51×10^{-8} and 3.55×10^{-6} m, respectively, and the maximum element growth rate was 1.4. Therefore, in 3D simulation for 6 μm and 12 μm AM particles, the numbers of tetrahedral elements were set at 615133 and 457737, respectively. The 3D simulations were also performed for a finer mesh of half the size, and similar results were obtained for battery performance. Therefore, the mesh convergence was confirmed by the output results. Using the Galerkin finite element method and the mesh size variation with position can reduce the computation cost of 3D simulations. Typical 3D simulations can take several hours, but our 3D simulations were performed in 6–20 min, for each C-rate. After the 3D ASSLiB model was meshed, 3D simulations were conducted using the equations mentioned in Section 2.2.1., for each tetrahedral mesh. The following boundary condition was used in equations (2)–(5), for the SE plane that faces outward in the y- and z-directions to prevent mass and charge leakage.

$$\vec{n} \cdot \nabla \phi = 0 \tag{9}$$

$\vec{n}$ is the normal vector. This boundary condition is based on the ASSLiB structure, where lithium transport predominantly occurs in the x-direction (through-plane direction). No unnatural transport behavior is observed due to the boundary condition, as the simulation results near the domain boundaries were consistent with those in the central region even at high C-rate discharge. The following boundary condition was used in equation (7), for the AM plane that faces outward from the cathode in the y- and z-directions.

$$\vec{n} \cdot \nabla c = 0 \tag{10}$$

3. Results and discussion

3.1. Comparison of the 3D simulation results with P2D simulation and experimental results

Fig. 3 shows the C-rate dependence on the discharge capacity for each cathode type ($D50_{AM}$ = 6 or 12 μm), obtained using experimental, P2D simulation, and 3D simulation methods. In Fig. 3(a) and (b), the red circles with solid lines represent the discharge capacity determined in the discharge experiment, the blue circles with solid lines represent the discharge capacity obtained in the P2D simulation, and the green circles with solid lines represent the discharge capacity obtained in the 3D simulation. Fig. 3(a) shows the results for the 6 μm median AM particle diameters, and Fig. 3(b) shows the results for the 12 μm median AM particle diameters. The plots show that the experimental discharge capacity decreases with increasing C-rate and $D50_{AM}$. The P2D simulation results qualitatively reproduce the decrease in discharge capacity with increasing C-rate and $D50_{AM}$, but not quantitatively. This quantitative differences between P2D simulation and experimental results originate from P2D models that rely on average structural parameters, which cannot account for particle size variation and asymmetric diffusion. The 3D simulations are more consistent with the experimental results. In 3D simulation, the cathode structure was adopted directly from X-ray CT

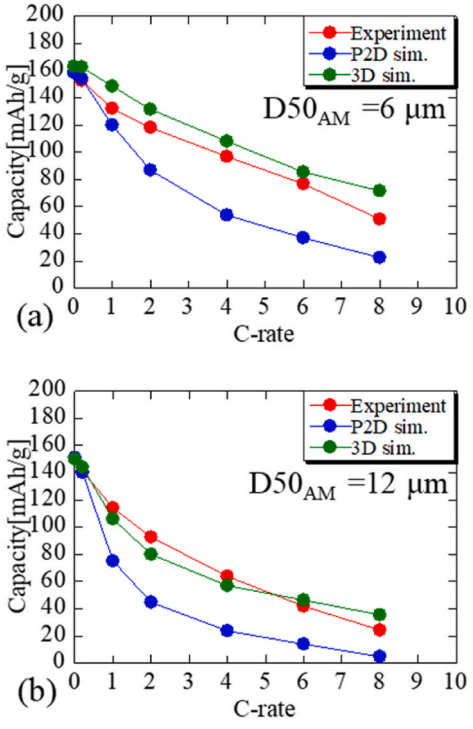

Fig. 3. C-rate dependence of the discharge capacity: (a) $D50_{AM}$ = 6 μm, (b) $D50_{AM}$ = 12 μm, for the experiment (red), P2D simulation (blue), and 3D simulation (green). (For interpretation of the references to colour in this figure legend, the reader is referred to the Web version of this article.)

images. While minor deviations may exist at the SE–cathode interface due to image trimming, this region is relatively small and has minimal influence on the overall simulation results. These findings indicate that the 3D simulations are valid because they can reflect the cathode structure, better captures the spatial inhomogeneities and particle-level configurations, enabling more realistic and accurate simulation of battery behavior.

Fig. 4 shows the discharge curves obtained at 0.1 ((a), (d)), 2 ((b), (e)) and 6C((c), (f)) for the two $D50_{AM}$ values, generated by experiments, P2D simulations, and 3D simulations. The red lines show the discharge curves with the experimental method, the blue lines represent the P2D simulation results, and the green lines represent the 3D simulation results. Fig. 4(a), (b), and (c) illustrate the results for the 6 μm AM particles, and Fig. 4(d), (e), and (f) show the results for the 12 μm AM particles. Fig. 4 shows that the discharge capacities obtained from experiments, P2D simulations, and 3D simulations decrease with the increasing C-rate and $D50_{AM}$, similar to the results shown in Fig. 3. The discharge curves at 0.1C exhibit a lower potential loss from the starting point than those at 6C. This is because the 0.1C discharge curves have a low IR overpotential in the SE and a low activation overpotential at the AM-SE interface because of the low current density. Additionally, the change in potential loss with the gradient of the discharge curves is due to the overpotential related to lithium diffusion in the AM, where the 0.1C discharge curves have a lower gradient than the 6C discharge curves. These results indicate that the discharge curves at 6C are more strongly influenced by the lithium diffusion overpotential. In Fig. 4, the discharge curves obtained by 3D and P2D simulations are almost consistent with the experimental results at 0.1C. This is because low overpotentials are generally reproduced at 0.1C, and the discharge curves represent the open-circuit voltage (OCV) curves. This confirms that using the actual electrode structures in the simulation does not have a significant impact on the results obtained at the lower C-rate (0.1C). However, the P2D simulation results differ from the experimental results at higher C-rates (2 and 6C), whereas the 3D simulation results remain consistent with the experimental results, especially the gradients of the discharge curves.

To help clarify the reason for the high precision of the 3D simulation or the discrepancy between the P2D simulation and the experimental results at the higher C-rate, overpotential isolation was performed on the discharge curves. Fig. 5 presents the overpotential isolation results for the OCV and 6C discharge curves using each $D50_{AM}$. Fig. 5(a) and (b) shows the results of 3D simulations for 6 and 12 μm AM particles, respectively. Fig. 5(c) and (d) shows the results of P2D simulations for 6 and 12 μm AM particles, respectively. The IR overpotential and activation overpotential were obtained from each simulation and calculated based on the ionic potential difference in the SE region near the anode and cathode. The activation overpotential was calculated from the sum of the potential difference at the AM-SE interface in the cathode and the lithium foil-SE interface in the anode. The overpotential related to lithium diffusion in the AM was determined by excluding the overpotential with IR overpotential and activation overpotential between the OCV and 6C discharge curves. In Fig. 5, the capacity reduction at the end of discharge due to IR overpotential and activation overpotential was low, which is similar to that at the end of the OCV curve. These results indicate that the capacity reduction is highly dependent on the overpotential related to lithium diffusion in the AM, which affects the gradient of the discharge curves. For the 6 μm median AM particle diameters, these capacity reductions are minimized, so lithium diffusivity is higher in the case of the smaller AM particles. The results of the 6 μm AM particles ((a), (c)) indicated that the overpotential with IR overpotential and activation overpotential are almost equal for both the 3D and P2D simulations. This is also observed for the 12 μm AM particles ((b), (d)). However, the overpotentials associated with lithium diffusion in the AM differ between the 3D and P2D simulations. P2D simulations used the structural parameters calculated from CT images, whereas 3D simulations incorporated the real electrode structure directly, going beyond the use of structural parameters to calculate internal phenomena. These results indicate that the 3D simulations, using the actual AM structure in the cathode, can reproduce the lithium diffusion overpotential more accurately than P2D simulations.

3.2. Lithium diffusion characteristics in AM based on 3D simulations

We found that the 3D simulation using the real electrode structure has high precision, as shown in Figs. 3–5. Next, we determined the lithium concentration distribution in the AM to discuss the lithium diffusion characteristics in actual AM structures using the 3D simulation model. Figs. 6 and 7 show the lithium concentration distributions obtained at 2 and 6C discharge in the real AM structures comprising each $D50_{AM}$, for the entire AM structure and cross-sections taken from parts of the AM structure. These cross-sections are composed of relatively small, medium, and large particle sizes. The entire AM structure shows the

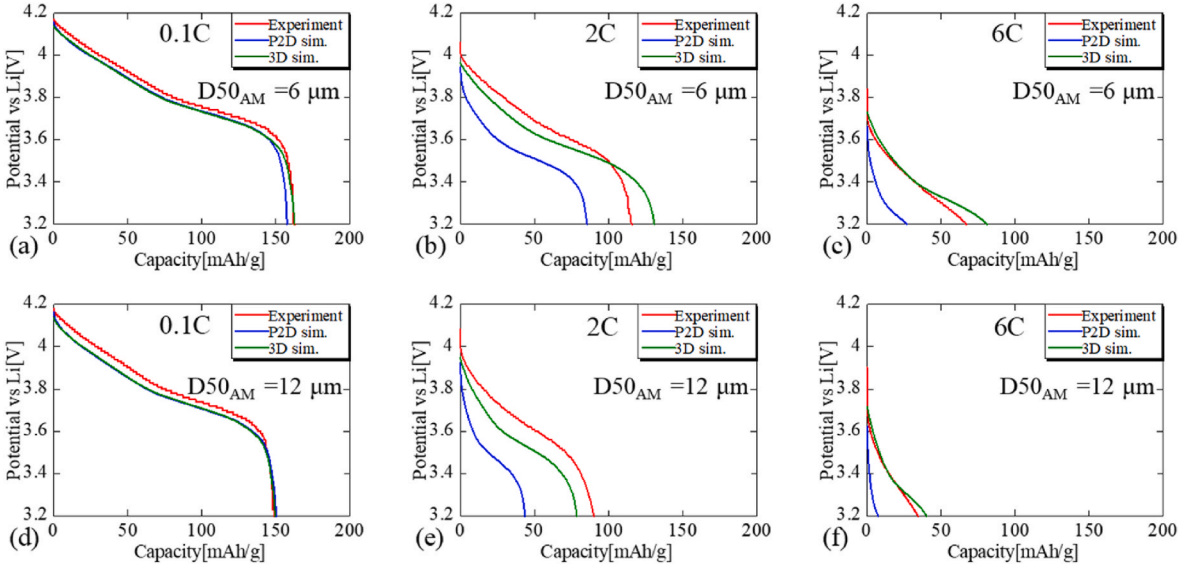

Fig. 4. The 0.1C discharge curves for experiments, P2D simulations, and 3D simulations using (a) $D50_{AM}$ = 6 μm and (d) $D50_{AM}$ = 12 μm; 2C discharge curves for experiments, P2D simulations, and 3D simulations using (b) $D50_{AM}$ = 6 μm and (e) $D50_{AM}$ = 12 μm; and 6C discharge curves for experiments, P2D simulations, and 3D simulations using (c) $D50_{AM}$ = 6 μm and (f) $D50_{AM}$ = 12 μm.

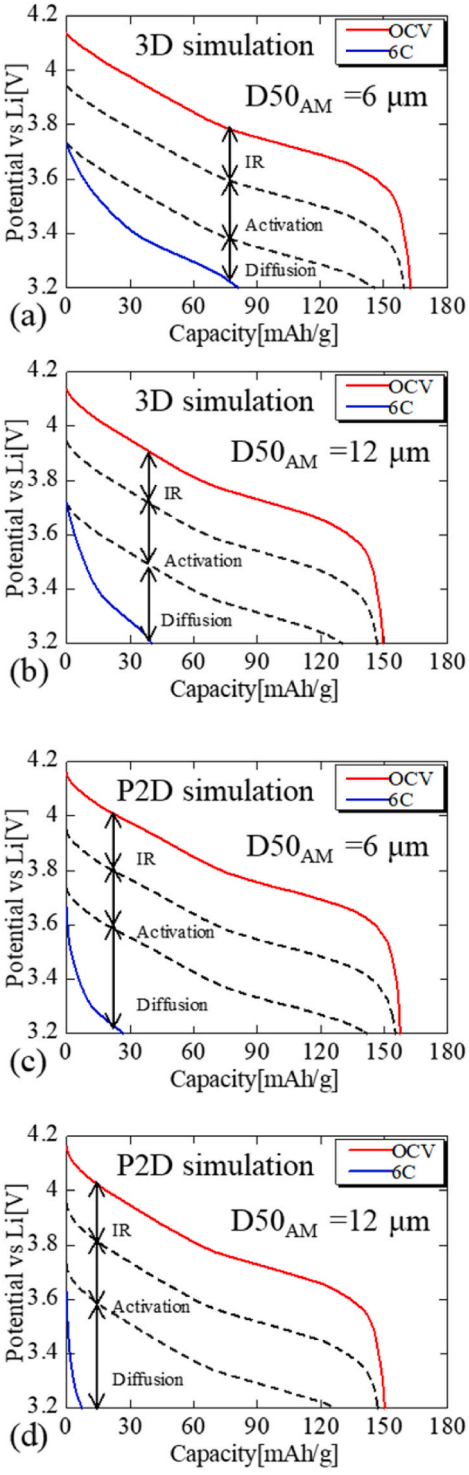

Fig. 5. Overpotential isolation between the OCV (red) and 6C (blue) discharge curves for (a) $D50_{AM}$ = 6 μm and (b) $D50_{AM}$ = 12 μm with 3D simulation, as well as (c) 50_{AM} = 6 μm and (d) $D50_{AM}$ = 12 μm with P2D simulation. (For interpretation of the references to colour in this figure legend, the reader is referred to the Web version of this article.)

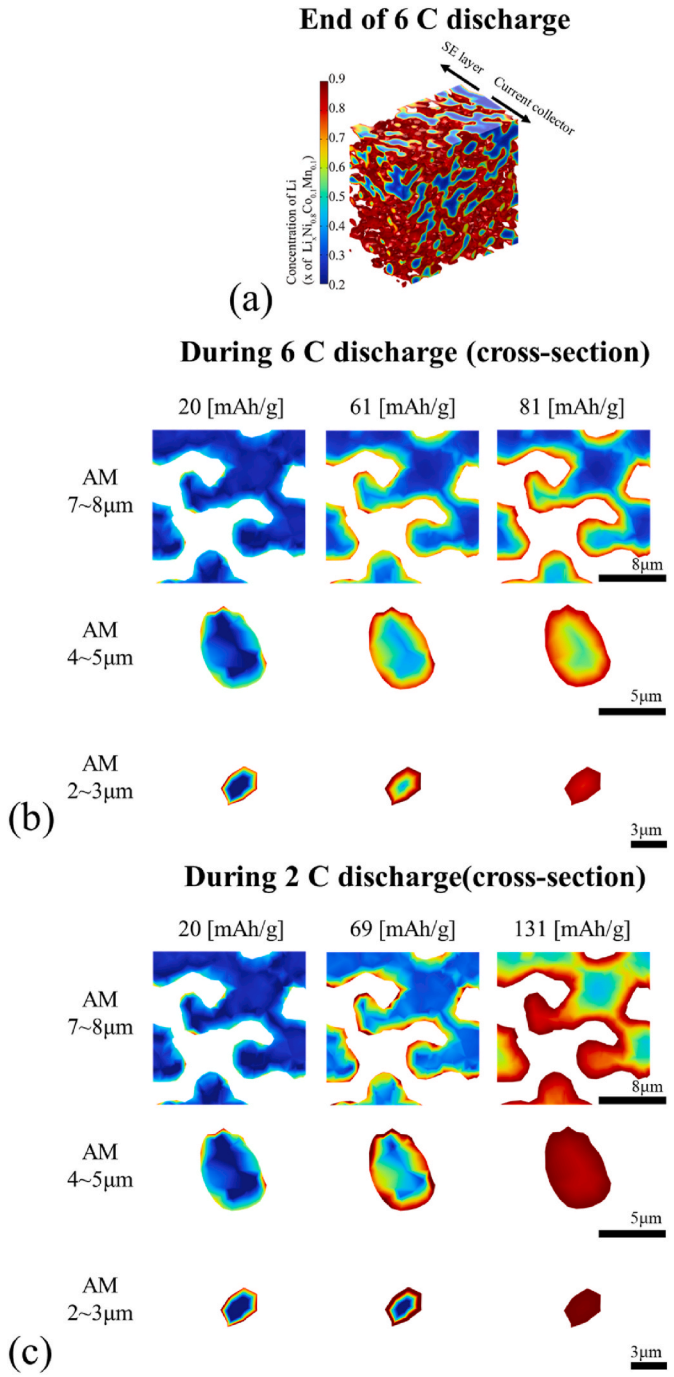

Fig. 6. 3D lithium concentration distribution across the entire electrode structure of the $D50_{AM}$ = 6 μm at the end of 6C discharge (a), and the cross-sectional lithium concentration distribution in AM particle deviation for $D50_{AM}$ = 6 μm electrode according to the change in discharge time of 6C discharge (b) and 2C discharge (c).

lithium concentration distribution at the end of the 6C discharge (Fig. 6 (a) and 7(a)). The cross-sections show the changes in the lithium concentration distribution with the increasing discharge time at 6C (Fig. 6 (b), 7(b)) and 2C (Fig. 6(c) and 7(c)). Fig. 6 shows the results of 6 μm AM particles, and Fig. 7 shows the results of 12 μm AM particles. Note that the lithium concentration is uniform across the entire AM structure surface in Fig. 6(a) and 7(a). This is because the SE in the electrode has sufficient ionic conductivity, and the electrode thickness is small enough that the lithium concentration distribution in the electrode direction is not evident. In contrast, the lithium concentration is inhomogeneous across the cross-sections in (b) and (c) of Figs. 6 and 7. These cross-sections show that lithium accumulated from the AM surface to the center as the discharge progressed. In the cross-section results at 6C (Fig. 6(b)), relatively large particles (7–8 μm) exhibit low lithium concentrations at the center, even when the discharge continued. Conversely, medium (4–5 μm) and small (2–3 μm) AM particles have

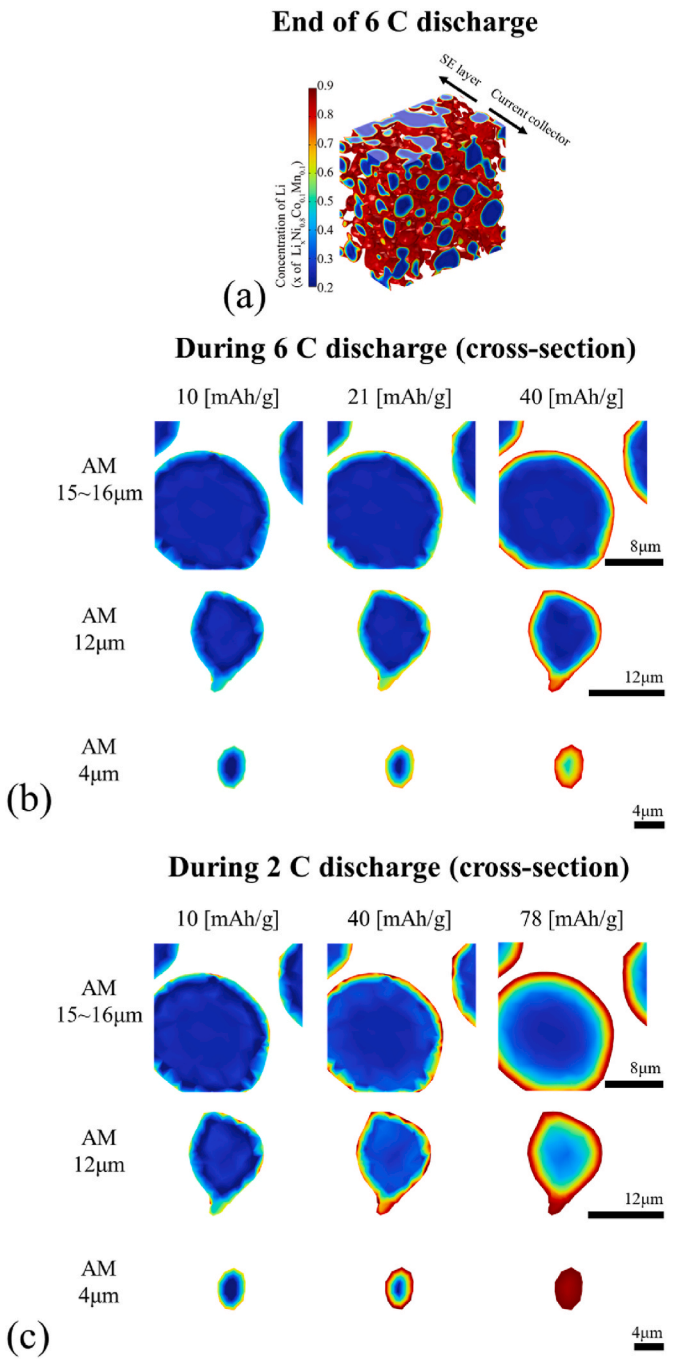

Fig. 7. 3D lithium concentration distribution across the entire electrode structure of the $D50_{AM}$ = 12 μm at the end of 6C discharge (a), and the cross-sectional lithium concentration distribution in AM particle deviation for $D50_{AM}$ = 12 μm electrode according to the change in discharge time of 6C discharge (b) and 2C discharge (c).

high lithium concentrations at the center. The lithium concentration on the AM surface is almost the same as that at the particle center, for the small AM particles. In the cross-section results at 2C (Fig. 6(c)), the small AM particle still has a high lithium concentration at the surface and center, whereas the large and medium AM particles have higher lithium concentrations than those observed in the corresponding 6C results. These findings indicated that the AM particles have higher lithium diffusivity at 2C owing to their lower overpotential, which is related to the lithium diffusion with low discharge speed. This trend can also be seen in Fig. 7(b) and (c). The cross-section results at 6C (Fig. 7(b)) indicate that the relatively large (15–16 μm) and medium (12 μm) AM particles accumulated lithium only on the surface as the discharge progressed, which resulted in the suppression of lithium diffusion to the center. Although the cross-sectional results for 2C in Fig. 7(c) show higher overall lithium concentrations than those for 6C, they exhibit a similar effect. In other words, the cross-section results in Fig. 7 indicate that only the relatively small AM particles (4 μm) exhibit discharge capacity, whereas the results in Fig. 6(b) and (c) indicate that both the small and medium AM particles contribute to the discharge capacity. The results of the electrode fabricated with smaller AM particle (Fig. 6) exhibit more uniform lithium distribution and higher discharge capacity due to more effective utilization of the entire particle volume. Especially in high C-rate conditions, this effect is noticeable, so reducing particle size is effective. This phenomenon is mainly attributed to diffusion overpotential rather than to the activation overpotential caused by interface resistance. Activation overpotential is almost the same for electrodes composed of either large or small particles. On the other hand, Smaller AM particles have a shorter diffusion distance from the interface to the center, resulting in a lower overpotential associated with Li diffusion. Hence, even if lithium is deposited on the AM-SE interface, the Li diffusivity increases, which leads to higher Li concentration in the AM particle center. However, in larger AM particles, lithium is accumulated near the surface and suppressed lithium diffusion to the center, causing higher overpotential. These findings investigate the direct relationship between particle size and diffusion-limited behavior in ASSLiBs, underscoring the importance of particle size optimization in cathode design. Moreover, the lithium concentration of smaller AM particles is higher in the center even with the same electrode. The 3D simulation results in this study demonstrate that it is important to consider particle size and its distribution in AM design. In particular, excessively large particles can lead to localized lithium accumulation, which negatively impacts overall battery performance. Therefore, minimizing particle size deviation is a key factor in ASSLiB performance, not just optimizing particle size. Ultimately, 3D simulations that can accurately calculate the device characteristics over long distances are expected to support more efficient battery development.

4. Conclusions

To enhance the performance of ASSLiBs, it is necessary to optimize the electrode structure through high-precision simulation. Although P2D simulations and some 3D simulations have been conducted, experimental results have not been extensively reproduced using simulations based on actual electrode structures. In this study, we developed a highly accurate 3D simulation method that incorporates complete electrode structures to investigate the effects of AM particle size on ASSLiB performance. Electrode structures with two different D50 a.m. particle sizes were obtained from X-ray CT images, and the validity of the 3D simulations was confirmed by comparing the results with experimental data and P2D simulations. The findings demonstrated that 3D simulations, which can fully account for AM particle size and shape deviations, show closer agreement with the experimental results than the P2D simulations, especially regarding the gradient of the discharge curves associated with the lithium diffusion overpotential in the AM at high C-rates. The 3D simulation results also suggested that smaller AM particles exhibit high lithium concentrations at the particle center even within the same electrode structure. As discharge progresses, a high lithium concentration accumulates on the AM particle surfaces, which blocks lithium diffusion into the center. However, smaller AM particles experience less impact from lithium accumulation owing to their shorter diffusion distances, resulting in lower lithium diffusion overpotentials and improved lithium diffusivity. Therefore, in addition to AM particle size, deviations in AM particle diameter significantly contribute to ASSLiB performance. Moreover, this 3D simulation method can be used to comprehensively evaluate the effects of real device structures on larger scales and supports further development of high-performance

batteries.

CRediT authorship contribution statement

K. Lee: Writing – original draft, Resources, Methodology, Investigation. **K. Yanagi:** Investigation, Data curation, Conceptualization. **T. Arashi:** Project administration. **M. Kodama:** Writing – review & editing, Supervision, Software, Project administration, Conceptualization.

Declaration of competing interest

The authors declare that they have no known competing financial interests or personal relationships that could have appeared to influence the work reported in this paper.

Acknowledgments

This work was supported by the Idemitsu Kosan Collaborative Research Cluster for Advanced Materials (IKCRCAM) in Tokyo Tech's open innovation platform. The authors would like to thank Prof. Takeshi Kikutani, the research director of IKCRCAM, for the useful discussions and the support of this work. This work is also supported by COMSOL Multiphysics (V6.2), and the authors would like to acknowledge the support of Keisoku Engineering System (KESCO) Co. Ltd. for their assistance throughout this research.

Data availability

Data will be made available on request.

References

[1] Y. Shen, Y. Zhang, S. Han, J. Wang, Z. Peng, L. Chen, Unlocking the energy capabilities of lithium metal electrode with solid-state electrolytes, Joule 2 (2018) 1674–1689, https://doi.org/10.1016/j.joule.2018.06.021.

[2] F. Lv, Z. Wang, L. Shi, J. Zhu, K. Edström, J. Mindemark, S. Yuan, Challenges and development of composite solid-state electrolytes for high-performance lithium ion batteries, J. Power Sources 441 (2019) 227175, https://doi.org/10.1016/j.jpowsour.2019.227175.

[3] W. Zhang, J. Nie, F. Li, Z.L. Wang, C. Sun, A durable and safe solid-state lithium battery with a hybrid electrolyte membrane, Nano Energy 45 (2018) 413–419, https://doi.org/10.1016/j.nanoen.2018.01.028.

[4] C.-L. Tsai, V. Roddatis, C.V. Chandran, Q. Ma, S. Uhlenbruck, M. Bram, P. Heitjans, O. Guillon, $Li_7 La_3 Zr_2 O_{12}$ interface modification for Li dendrite prevention, ACS Appl. Mater. Interfaces 8 (2016) 10617–10626, https://doi.org/10.1021/acsami.6b00831.

[5] X.-B. Cheng, R. Zhang, C.-Z. Zhao, Q. Zhang, Toward safe lithium metal anode in rechargeable batteries: a review, Chem. Rev. 117 (2017) 10403–10473, https://doi.org/10.1021/acs.chemrev.7b00115.

[6] M. Doyle, J. Newman, The use of mathematical modeling in the design of lithium/polymer battery systems, Electrochim. Acta 40 (1995) 2191–2196, https://doi.org/10.1016/0013-4686(95)00162-8.

[7] N. Wolff, F. Röder, U. Krewer, Model based assessment of performance of lithium-ion batteries using single ion conducting electrolytes, Electrochim. Acta 284 (2018) 639–646, https://doi.org/10.1016/j.electacta.2018.07.125.

[8] W. Ai, Y. Liu, Improving the convergence rate of Newman's battery model using 2nd order finite element method, J. Energy Storage 67 (2023) 107512, https://doi.org/10.1016/j.est.2023.107512.

[9] S. Iwamoto, M. Kodama, K. Yanagi, Y. Haniu, Y. Fujii, N. Masuda, H. Higuchi, Y. Suetsugu, S. Hirai, Numerical simulations of all-solid-state batteries using specific contact area diameters for active materials determined by X-ray computed tomography, Journal of Power Sources Advances 21 (2023) 100120, https://doi.org/10.1016/j.powera.2023.100120.

[10] K. Lee, M. Kodama, K. Yanagi, Y. Haniu, H. Higuchi, T. Arashi, S. Hirai, Active material particle size effects on all-solid-state Li-ion batteries via X-ray CT based simulations, J. Electrochem. Soc. 171 (2024) 110529, https://doi.org/10.1149/1945-7111/ad94aa.

[11] A. Bielefeld, D.A. Weber, J. Janek, Microstructural modeling of composite cathodes for all-solid-state batteries, J. Phys. Chem. C 123 (2019) 1626–1634, https://doi.org/10.1021/acs.jpcc.8b11043.

[12] A. Bielefeld, D.A. Weber, J. Janek, Modeling effective ionic conductivity and binder influence in composite cathodes for all-solid-state batteries, ACS Appl. Mater. Interfaces 12 (2020) 12821–12833, https://doi.org/10.1021/acsami.9b22788.

[13] M. So, G. Inoue, K. Park, K. Nunoshita, S. Ishikawa, Y. Tsuge, Simulation of the compaction of an all-solid-state battery cathode with coated particles using the discrete element method, J. Power Sources 530 (2022) 231279, https://doi.org/10.1016/j.jpowsour.2022.231279.

[14] S. Yamakawa, S. Ohta, T. Kobayashi, Effect of positive electrode microstructure in all-solid-state lithium-ion battery on high-rate discharge capability, Solid State Ionics 344 (2020) 115079, https://doi.org/10.1016/j.ssi.2019.115079.

[15] P. Huang, L.T. Gao, Z.-S. Guo, Electrochemo-mechanical response of all solid-state batteries: finite element simulations supported by image-based 3D reconstruction of X-ray microscopy tomography, Electrochim. Acta 463 (2023) 142873, https://doi.org/10.1016/j.electacta.2023.142873.

[16] H. Fathiannasab, A. Ghorbani Kashkooli, T. Li, L. Zhu, Z. Chen, Three-dimensional modeling of all-solid-state lithium-ion batteries using synchrotron transmission X-ray microscopy tomography, J. Electrochem. Soc. 167 (2020) 100558, https://doi.org/10.1149/1945-7111/ab9380.

[17] M. Finsterbusch, T. Danner, C.-L. Tsai, S. Uhlenbruck, A. Latz, O. Guillon, High capacity garnet-based all-solid-state lithium batteries: fabrication and 3D-microstructure resolved modeling, ACS Appl. Mater. Interfaces 10 (2018) 22329–22339, https://doi.org/10.1021/acsami.8b06705.

[18] M. Kodama, A. Ohashi, H. Adachi, T. Miyuki, A. Takeuchi, M. Yasutake, K. Uesugi, T. Kaburagi, S. Hirai, Three-dimensional structural measurement and material identification of an all-solid-state lithium-ion battery by X-Ray nanotomography and deep learning, Journal of Power Sources Advances 8 (2021) 100048, https://doi.org/10.1016/j.powera.2021.100048.

[19] Y. Takase, M. Kodama, R. Iwamura, H. Kawakami, K. Aotani, Y. Aihara, S. Hirai, Effects of solid electrolyte particle size and silver-carbon interlayer on lithium deposition in all-solid-state lithium-metal batteries, Electrochim. Acta 498 (2024) 144670, https://doi.org/10.1016/j.electacta.2024.144670.

[20] H. Wang, C. Yu, S. Ganapathy, E.R.H. Van Eck, L. Van Eijck, M. Wagemaker, A lithium argyrodite Li6PS5Cl0.5Br0.5 electrolyte with improved bulk and interfacial conductivity, J. Power Sources 412 (2019) 29–36, https://doi.org/10.1016/j.jpowsour.2018.11.029.

[21] B. Tjaden, S.J. Cooper, D.J. Brett, D. Kramer, P.R. Shearing, On the origin and application of the Bruggeman correlation for analysing transport phenomena in electrochemical systems, Curr. Opin. Chem. Eng. 12 (2016) 44–51, https://doi.org/10.1016/j.coche.2016.02.006.

[22] A. Tron, A. Orue, P. López-Aranguren, A. Beutl, Critical current density measurements of argyrodite $Li_6 PS_5 Cl$ solid electrolyte at ambient pressure, J. Electrochem. Soc. 170 (2023) 100525, https://doi.org/10.1149/1945-7111/ad01e3.

[23] T.E. Ashton, P.J. Baker, C. Sotelo-Vazquez, C.J.M. Footer, KenjiM. Kojima, T. Matsukawa, T. Kamiyama, J.A. Darr, Stoichiometrically driven disorder and local diffusion in NMC cathodes, J. Mater. Chem. A 9 (2021) 10477–10486, https://doi.org/10.1039/D1TA01639C.

[24] R. Ruess, S. Schweidler, H. Hemmelmann, G. Conforto, A. Bielefeld, D.A. Weber, J. Sann, M.T. Elm, J. Janek, Influence of NCM particle cracking on kinetics of lithium-ion batteries with liquid or solid electrolyte, J. Electrochem. Soc. 167 (2020) 100532, https://doi.org/10.1149/1945-7111/ab9a2c.

[25] A. Ohashi, M. Kodama, N. Horikawa, S. Hirai, Effect of Young's modulus of active materials on ion transport through solid electrolyte in all-solid-state lithium-ion battery, J. Power Sources 483 (2021) 229212, https://doi.org/10.1016/j.jpowsour.2020.229212.

[26] M. Kodama, S. Komiyama, A. Ohashi, N. Horikawa, K. Kawamura, S. Hirai, High-pressure in situ X-ray computed tomography and numerical simulation of sulfide solid electrolyte, J. Power Sources 462 (2020) 228160, https://doi.org/10.1016/j.jpowsour.2020.228160.